RESEARCH ARTICLE

Comparative Study on the Radial Force and Acoustic Noise Harmonics of an Interior Permanent Magnet, Induction, and Switched Reluctance Motor Drive

MOIEN MASOUMI, (Graduate Student Member, IEEE),
AND BERKER BILGIN, (Senior Member, IEEE)
McMaster Automotive Resource Center, McMaster University, Hamilton, ON L8P 0A6, Canada

Corresponding author: Moien Masoumi (masoum6@mcmaster.ca)

ABSTRACT The demand for electrical machines has been spurred by rising fuel costs, technological advancements, and urbanization. Consequently, there is an increased focus on developing machines with greater power density, improved efficiency, and enhanced vibroacoustic characteristics while promoting a more sustainable supply chain. This paper offers a thorough comparison of three distinct motor topologies: switched reluctance motor (SRM), interior permanent magnet synchronous motor (IPMSM), and induction motor (IM). The study begins with electromagnetic analysis of the motors, covering torque, output power, losses, and efficiency calculations. Subsequently, the investigation delves into radial force density wave-forms, extracting the dominant radial force density harmonics and presenting patterns for each motor's dominant radial force harmonics. Following this, a 3D assembly of the motors is introduced for modal analysis, determining their mode shapes and natural frequencies. Finally, vibroacoustic analysis is conducted for the proposed motors, with observed differences being discussed. These analyses are conducted solely for the rated operating point, as transitioning to other operating points does not alter the pattern of radial force harmonics or the correlation between acoustic noise and radial force harmonics.

INDEX TERMS Electromagnetic performance, induction motor, interior permanent magnet motor, radial force harmonics, sound pressure level, switched reluctance motor, vibroacoustic analysis.

I. INTRODUCTION

In recent years, there has been a noticeable surge in the demand for electric motors across various sectors like automotive, industrial, and residential, and this trend is expected to continue in the following years. This surge can be attributed to a range of factors, including technological progress, the integration of automation into industrial operations, elevated fuel costs, and the ongoing trend of urbanization [1], [2].

The adoption of Permanent Magnet (PM) machines has significantly grown across diverse applications, driven by technological advancements such as rapid computing and the

The associate editor coordinating the review of this manuscript and approving it for publication was Yi Ren.

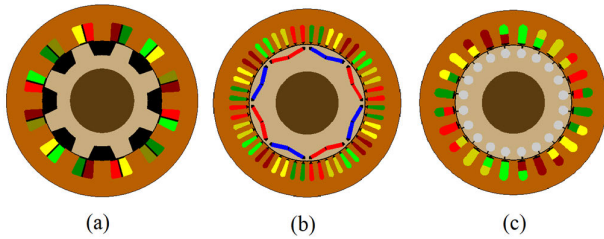widespread availability of commercial Finite Element Analysis (FEA) software, coupled with the increased accessibility of high-energy PMs. Within this context, IPMSMs have seen widespread acceptance due to their notable attributes of high efficiency, high power density, and dependable operation [3], [4]. However, the supply and accessibility of PMs are constrained by factors like price fluctuations and environmental concerns [1]. In contrast, both IMs and SRMs steer clear of PM usage. While IMs benefit from a well-established design and have a long history of industrial application, they may necessitate additional cooling due to higher rotor losses. SRMs are presented as an alternative to IMs and IPMSMs. They offer a simplified design, robustness, and capability to operate at elevated temperatures and speeds. Nonetheless,

FIGURE 1. Proposed motors (a) 12/8 SRM (b) 48/8 IPMSM (c) 24/20 IM.

TABLE 1. Mechanical specifications of the analyzed motors.

Parameter	SRM	IPMSM	IM
Stator outer diameter [mm]	210	210	210
Rotor outer diameter [mm]	130	130	130
Stack length [mm]	120	75	120
Air gap length [mm]	0.4	0.6	0.5
Shaft diameter [mm]	70	70	70
Stator core weight [kg]	15.1	9.4	14.8
Stator copper weight [kg]	3.4	4.2	4.8
Rotor core weight [kg]	5.7	4.7	8.8
Rotor bar and ring weight [kg]	---	---	1.6
Magnet weight [kg]	---	0.6	---
Total weight [kg]	24.2	18.9	30
Steel lamination	M300-35A	M300-35A	M300-35A

SRMs present challenges such as lower torque and power density, increased torque ripple, and higher noise levels [5], [6], [7]. To better illustrate the distinctive characteristics of these three motor types, the existing literature has undertaken several comparative analyses. A comprehensive assessment of the electromagnetic capabilities across different motor types suitable for HEV/EV applications is detailed in [8]. This assessment is grounded in torque-speed characteristics, efficiency maps, and drive cycle efficiency. Another study in [9], introduces a spoke-type IPMSM and an IM as potential alternatives to a second-generation Prius-IPMSM. A thorough examination and comparison were conducted on these options, with a specific focus on current angle control throughout the complete torque-speed envelope. For a hybrid truck application, three distinct motors, including an SRM and an IPMSM, were designed and optimized in [10]. A comparative evaluation utilizing the Pugh matrix takes into account factors such as cost, efficiency, power density, fault tolerance, and manufacturability. Performance comparison of three motors including an IPMSM and an IM is presented in [11] for the same motor core volume, inverter size, and cooling system. The study establishes analytical relationships, subsequently validated through practical design instances. Extending the scope, in [12], a thorough comparison was proposed among different motor types, SRM, IPMSM, and IM, customized for an EV application. The study utilizes MATLAB/Simulink simulations to explore the electromagnetic performance of these motors, thereby deepening insights into their distinct capabilities.

While electromagnetic analysis is necessary for understanding the electrical aspects of electric motors, vibroacoustic analysis is important to ensure optimal user experience, mechanical integrity, and compliance with regulations [13], [14]. Acoustic noise and vibration reduction are among the factors that are considered in the design process of electrical machines [15]. The design and control of electrical machines to tackle acoustic noise and vibration are typically approached through two primary methods, namely structural design [16], [17], [18] and control techniques [19], [20], [21], [22]. However, before devising strategies for mitigating these noise and vibration concerns, it is important to thoroughly analyze and comprehend the vibroacoustic characteristics inherent in electric machines. Combining both electromagnetic and Noise, Vibration, and Harshness (NVH) analyses

leads to a comprehensive understanding of electric motor behavior and helps engineers analyze the impact of electromagnetic forces on motor noise.

The majority of comparative studies in the electric motors field have primarily focused on electromagnetic performance. Only a limited number of studies have taken into account vibroacoustic characteristics, such as radial force harmonics, vibrations, and motor noise levels. In [5], a comparison is made among SRM, IPMSM, and IM motor drives for EV/HEV applications. This study thoroughly examines the suggested motors from an electromagnetic perspective. In addition, it discusses the radial force harmonics and natural frequencies. However, there exists a gap in the comprehensive analysis of vibroacoustic aspects. This study compares three different motor topologies: SRM, IPMSM, and IM. The primary emphasis of this paper lies in conducting an in-depth investigation into the harmonic content of the radial force and vibroacoustic characteristics of the motors. The rated operating point is considered for the analyses because transitioning to other operating points does not alter the pattern of radial force harmonics or the relationship between acoustic noise and radial force harmonics. The paper is structured into multiple sections. Section II presents the electromagnetic simulation and analysis conducted on the motors. In Section IV, the discussion revolves around the radial force, radial force harmonics, and their interrelation with machine parameters. Section V encompasses the mechanical assembly, modal analysis, and vibroacoustic analysis. Finally, Section V provides the conclusions.

II. ELECTROMAGNETIC SIMULATION AND ANALYSIS

The study compares three different motor topologies: a 12/8 SRM (12 stator poles, 8 rotor poles), a 48/8 IPMSM (48 stator slots, 8 poles), and a 24/20 IM (24 stator slots, 20 rotor bars, 4 poles). Fig. 1 displays the motor cross-sections. The SRM utilizes a three-phase concentrated winding, while

TABLE 2. Electrical specifications of the analyzed motors.

Parameter	SRM	IPMSM	IM
Rated torque (Nm)	41.9	53.9	46.6
Rated power (kW)	7.90	10.16	8.78
Rated speed (rpm)	1800	1800	1800
Current density (A/mm^2)	3.6	3.6	3.6
Maximum phase current (A)	63.5	59.9	53.1
Core loss (W)	133	47	65
Copper loss (W)	358	810	742
Efficiency (%)	94.1	92.2	91.4
Torque ripple (%)	38.9	26.3	30.0

the IPMSM and IM employ three-phase single-layer and double-layer distributed windings, respectively.

Tables 1 and 2 present the specifications and performance of the motors analyzed in this study. The motors are not designed competitively in terms of performance, but they are considered in a way that their electromagnetic and acoustic characteristics are comparable. They share the same outer diameter, electrical steel lamination, and current density. The motors are not designed to achieve the same power density, and they have different stack lengths.

The electromagnetic simulations of the examined motors were performed using Flux software, specifically for the rated operating point. The decision to concentrate exclusively on this operating point is grounded in the fact that altering to other points does not impact the pattern of radial force harmonics or the correlation between acoustic noise and radial force harmonics, which is the central focus of this study. For the SRM, the static characteristics are extracted from Flux as look-up tables. Subsequently, an offline modeling is employed in MATLAB/Simulink, utilizing these look-up tables to compute the dynamic characteristics. The dynamic model is utilized to calculate optimal turn-on and turn-off angles, aiming to attain maximum torque. In the case of IPMSM, a Maximum Torque per Ampere (MTPA) control strategy is implemented to determine the optimal current angle for maximizing the torque. For the IM, the torque-slip characteristic is determined through steady-state analysis and serves as an initial condition for transient analysis at the rated speed.

III. RADIAL FORCE HARMONICS

The electromagnetic radial force, which changes with time and spatial position is one of the major sources of vibration and acoustic noise in electric machines [24], [25]. The electromagnetic radial force can be conceptualized as a surface wave that changes over time and across space. Such a time- and space-changing surface wave can be described as:

$$d(t, \alpha) = A \cos(\omega_u t + \vartheta \alpha + \varphi) \quad (1)$$

where A is the magnitude of the surface wave, t is time, α is the spatial position, φ is the phase angle, u is the temporal

order, and ϑ is the spatial or circumferential order [26]. Equation (1) can be rewritten as:

$$d(t, \alpha) = A \cos(2\pi u f_{mech} t + \vartheta \alpha + \varphi) \quad (2)$$

where f_{mech} is the mechanical frequency. The Maxwell stress tensor can be employed to calculate the radial force density as:

$$\sigma_{rad}(t, \alpha) = \frac{1}{2\mu_0} \left[\beta_r^2(t, \alpha) - \beta_t^2(t, \alpha) \right] \quad (3)$$

where β_r and β_t are the radial and tangential elements of the magnetic flux density. To determine β_r and β_t, a line support is established within the airgap of the motor, comprising a specific number of nodes. Subsequently, β_r and β_t are computed at these nodes following the completion of the electromagnetic simulation. Increased node count enhances the precision of radial force calculations.

Figs. 2, 3, and 4 illustrate the 2D radial force density waveforms of the compared motors concerning rotation angle (time) and circumferential position. Additionally, with each radial force density plot, 1D radial force density waveforms for a given time instant and circumferential position are illustrated. The waveforms of radial force density can be represented by the Fourier series as:

$$\sigma_{rad}(t, \alpha) = \sum_{u=-\infty}^{\infty} \sum_{\vartheta=-\infty}^{\infty} F_{u,\vartheta} \cos(u\omega_m t + \vartheta \alpha + \varphi_{u,\vartheta}) \quad (4)$$

where $F_{u,\vartheta}$ is the amplitude, u is the temporal order, and ϑ is the spatial order [26].

The temporal order (u) determines the frequency of a force component. For a harmonic with a temporal order of u, the corresponding forcing frequency is $|u|$ times f_{mech}. The spatial order (ϑ) defines the shape of the force component. The mode shapes are excited by the spatial orders of the same shape at different frequencies, which are defined by the temporal order. Higher spatial orders of radial force harmonics may also excite the vibration modes with lower circumferential modes due to the sampling effect [27]. Fig. 5 illustrates the harmonic spectrum of radial force density for the proposed motors. These spectra are derived through the application of a 2D Fast Fourier Transform (FFT) to the waveforms of radial force density. Due to the distinct factors influencing the radial force harmonics in the motors, it is essential to conduct separate investigations for each motor topology.

A. SRM

Based on the radial force waveform in Fig. 2(a), the quantity of magnetic poles (the number of stator poles divided by the number of phases) is expected to appear on the spatial order, and the impact of the quantity of rotor poles is anticipated on the temporal order of the harmonic content. In the 12/8 SRM, the number of magnetic poles is four. Therefore, when the radial force is plotted for a single time step and all circumferential positions, as shown in Fig 2(b), four distinct
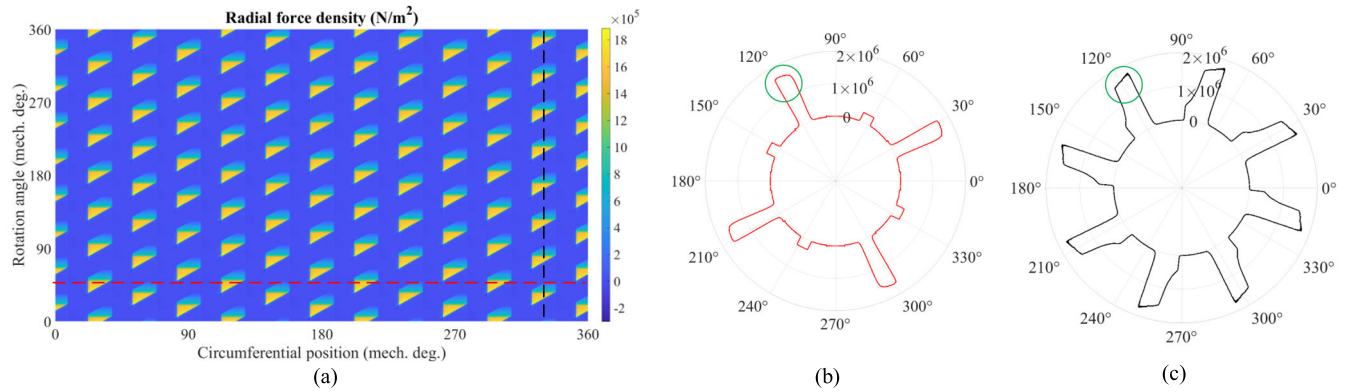
FIGURE 2. Radial force density waveform of SRM as a function of rotation angle and circumferential position, (b) Polar plot of SRM radial force as a function of circumferential position at a constant rotation angle, (c) Polar plot of SRM radial force as a function of rotation angle at a constant circumferential position.
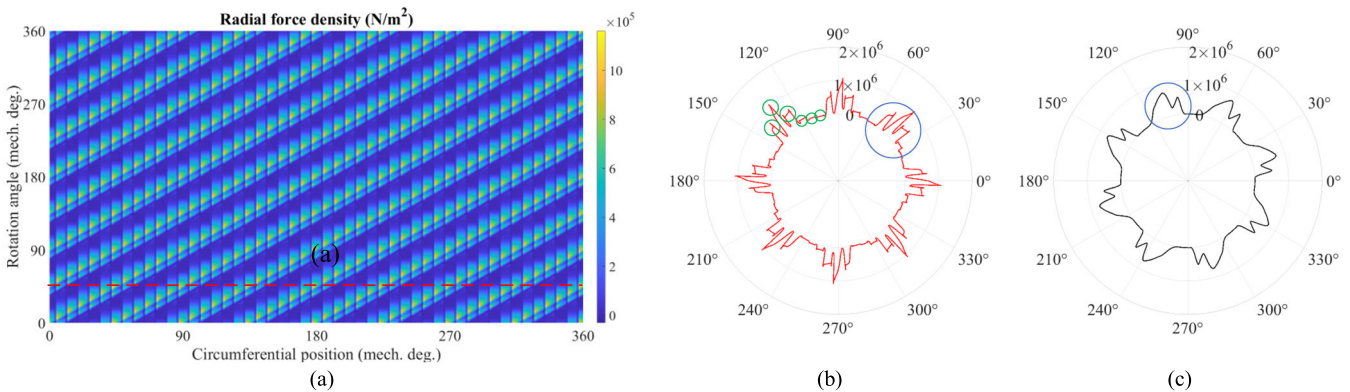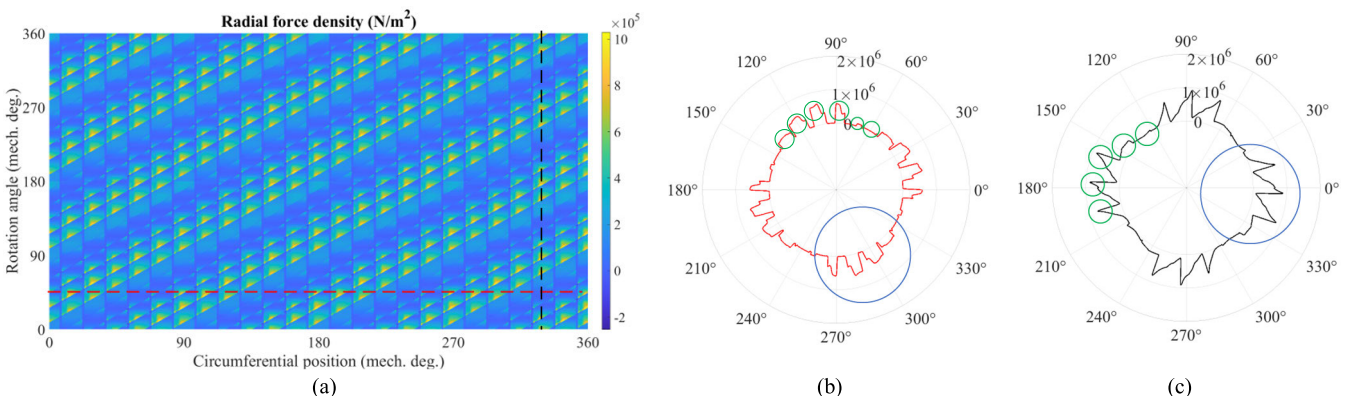

FIGURE 3. Radial force density waveform of IPMSM as a function of rotation angle and circumferential position, (b) Polar plot of IPMSM radial force as a function of circumferential position at a constant rotation angle, (c) Polar plot of IPMSM radial force as a function of rotation angle at a constant circumferential position.

FIGURE 4. (a) Radial force density waveform of IM as a function of rotation angle and circumferential position, (b) Polar plot of IM radial force as a function of circumferential position at a constant rotation angle, (c) Polar plot of IM radial force as a function of rotation angle at a constant circumferential position.

peaks appear. One of these peaks is identified with a green circle in this figure. The presence of four smaller peaks is due to the overlap between the conduction of two phases. There are eight rotor poles. Hence, when the radial force

is plotted for one circumferential position and for all time instants, as shown in Fig. 2(c), eight peaks are identified. One of these peaks is identified with a green circle in this figure. A pattern can be established to describe the temporal

and spatial orders of the radial force harmonics in an SRM, which can be articulated as:

$$(u, \vartheta) = \left(N_{ph} \times N_r \times k_1 + N_r \times k_2, N_s/N_{ph} \times k_2\right)$$
$$= (24k_1 + 8k_2, 4k_2)$$
$$k_1, k_2 = 0, \pm1, \pm2, \dots \tag{5}$$

where N_{ph} is the number of phases, N_s is the number of the stator poles, and N_r is the number of the rotor poles.

B. IPMSM

In Fig. 3(a), the number of poles of the IPMSM exhibits a diagonal pattern within the radial force waveform. The 48/8 IPMSM has eight poles. The red line in Fig. 3(a) is drawn at a certain time instant and it crosses eight diagonals over the entire circumferential position. Similarly, the black line in Fig.3(a) is drawn at a certain circumferential position and it crosses eight diagonals over the entire range of time. Therefore, the number of poles impacts both the temporal and spatial orders. The impact of the number of poles can also be noted in the 1D polar plots in Fig. 3(b) and Fig. 3(c). Both have patterns of eight. One of these patterns is identified with a blue circle in both polar plots. The number of stator slots is equal to 48. Hence, if the radial force is plotted for a single time step and all the circumferential positions, as shown in Fig. 3(b), 48 oscillations are identified. One-eighth of these oscillations (six oscillations) are identified with green circles in this figure. A pattern can be established to describe the temporal and spatial orders of the dominant radial force harmonics in an IPMSM, and it can be expressed as:

$$(u, \vartheta) = \left(2 \times p_p \times k_1, -2 \times p_p \times k_1 + N_s/2 \times k_2\right)$$
$$= (8k_1, -8k_1, 24k_2)$$
$$k_1, k_2 = 0, \pm1, \pm2, \dots \tag{6}$$

where p_p is the number of pole pairs, and N_s is the number of stator slots.

C. IM

In the case of the IM, three factors influence the harmonic composition of the radial force, making it more complicated to quantify the harmonic order as compared to SRM and IPMSM. These three factors are the number of pole pairs (p_p), the number of stator slots (N_s), and the number of rotor bars (N_r). Both temporal and spatial orders are influenced by the number of poles and rotor bars, revealing themselves as diagonal patterns within the radial force waveform, as shown in Fig. 4(a). In a 24/20 IM, the number of poles is four. Hence, in both polar plots in Fig. 4(b) and Fig 4(c), four patterns are identified with a blue circle. In addition, the number of rotor bars is 20. Hence, if the radial force is plotted for one circumferential position and for all time instants, as shown in Fig. 4(c), 20 oscillations are identified. One-fourth of these oscillations (five oscillations) are identified with green circles in this figure. Counting 20 oscillations in the red polar plot in Fig. 4(b) can be challenging due to the combined impact
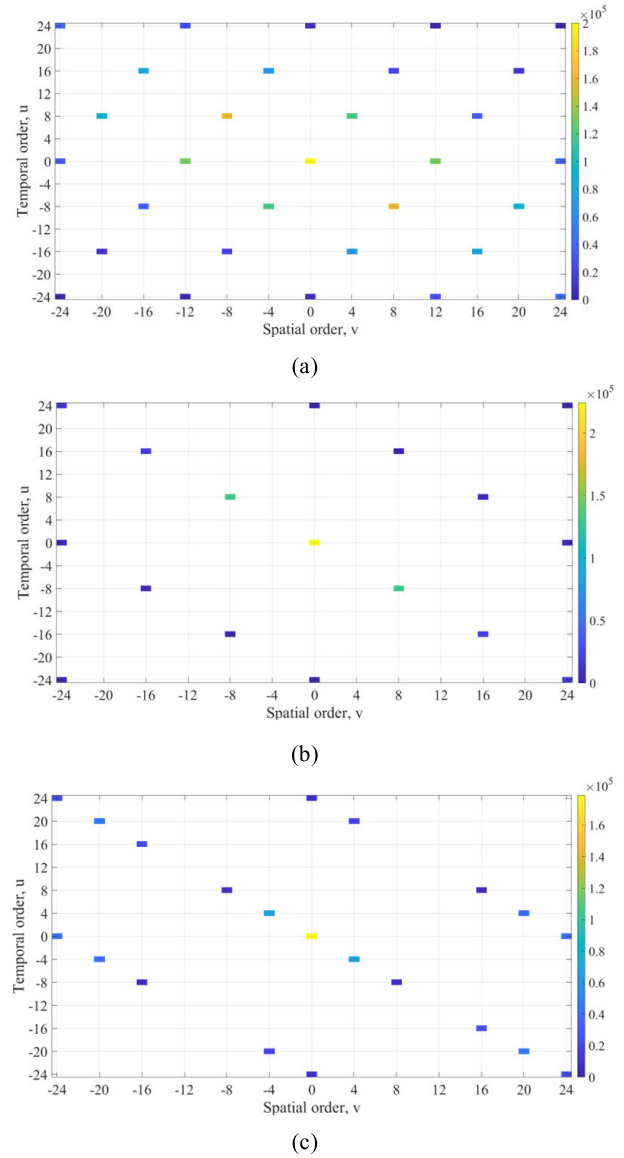

(a)

(b)
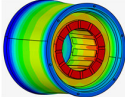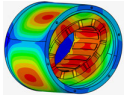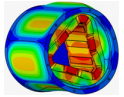

(c)

FIGURE 5. Radial force harmonics (a) SRM (b) IPMSM (c) IM.
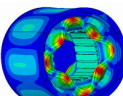
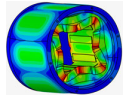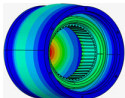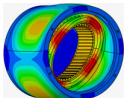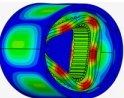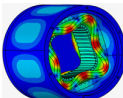of the number of rotor bars and stator slots in this plot. It is anticipated that the number of stator slots solely affects spatial order due to its alignment with a vertical pattern. In a 24/20 IM, there are 24 stator slots, and 24 oscillations can be counted in Fig 4 (b) which shows the 1D radia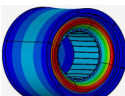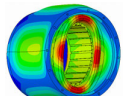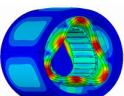l force for a single time step and all the circumferential positions. One-fourth of these oscillations (six oscillations) are identified with green circles in this figure. A pattern can be established to describe the temporal and spatial orders of the radial force harmonics in an IM, which can be articulated as follows:

$$(u, \vartheta) = (2 \times p_p \times k_1 + N_r \times k_2,$$
$$-2 \times p_p \times k_1 - N_r \times k_2 + N_s/2 \times k_3)$$
$$= (4k_1 + 20k_2, -4k_1 - 20k_2 + 12k_3)$$
$$k_1, k_2, k_3 = 0, \pm1, \pm2, \dots \tag{7}$$

TABLE 3. Material properties of the structure.

Part	Housing and endcaps	Stator	Winding
Material	Aluminum	M300-35A steel	Magnet wire
Density [kg/m3]	2700	7220	4120
Young's modulus [GPa]	68.9	176	13
Poisson's ratio	0.33	0.3015	0.3

TABLE 4. Mode shapes and natural frequencies of the proposed motors.

Mode 0	Mode 2	Mode 3	Mode 4
SRM			
7269 Hz	3021 Hz	5993 Hz	9605 Hz
IPMSM			
6200 Hz	2648 Hz	5027 Hz	7817 Hz
IM			
7375 Hz	2837 Hz	5346 Hz	9430 Hz

It can be observed that an SRM, IPMSM, and IM have distinct radial force patterns determined by their construction and excitation. In the SRM and IPMSM, the harmonics with lower temporal or spatial orders (e.g., closer to the DC component) exhibit a higher magnitude. In the IM, the dominant radial force components are more distributed. The harmonics with lower temporal or spatial orders (closer to the DC component) exhibit a higher magnitude in the SRM and IPMSM. The IM displays a distinct pattern, with the dominant radial force component being more distributed. This divergence arises due to the combined impact of the number of pole pairs (p_p), the number of stator slots (N_s), and the number of rotor bars (N_r).

IV. VIBROACOUSTIC SIMULATION AND ANALYSIS

The radial force harmonics calculated for each motor are employed to compute the acoustic noise harmonics. Fig. 6 illustrates the workflow of the vibroacoustic modeling and analysis conducted through numerical methods. To perform vibroacoustic simulation, essential inputs such as
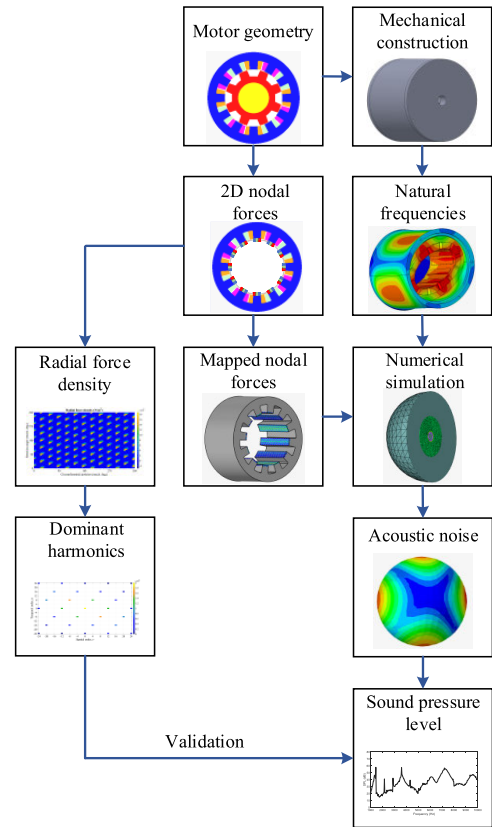

FIGURE 6. Workflow diagram for the modeling and analysis of the acoustic noise.

electromagnetic nodal forces, 3D meshing of the motor structure, and modal properties are necessary. The 3D meshing, modal analysis, and vibroacoustic analysis are performed within the Altair Simlab software. Electromagnetic nodal forces are extracted from Altair Flux models of each motor and mapped to the 3D mesh. The following two subsections will delve into the modal and vibroacoustic modeling and analysis of the analyzed motors.

A. MODAL ANALYSIS

Each vibration mode of an electric motor usually has a specific mode shape and natural (modal) frequency. The shape, dimensions, and installation constraints of the motor can influence these vibration modes. An electric motor has a complex structure encompassing the housing, stator, winding, and endcaps. Hence, it can exhibit multiple vibration modes in axial, circumferential, and twisting directions, as well as combinations thereof. However, because of the nature of electromagnetic force density within an electric motor, most of the modes cannot be excited. Generally, axial mode one and different circumferential modes are the ones that can be excited [28].

To conduct modal analysis, 3D structures of the motors, encompassing components such as the housing, endcaps, stator, and winding, are developed. The housing and endcaps
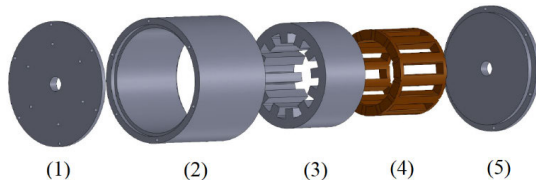
FIGURE 7. Exploded view of the analyzed SRM (1) front endcap (2) housing (3) stator (4) winding (5) rear endcap.

TABLE 5. Calculated damping ratio values.

	Mode 0	Mode 4	Average
SRM	4.18	5.20	4.69
IPMSM	3.71	---	3.71
IM	4.23	5.13	4.68

FIGURE 8. Structural meshing, near field, and far field in numerical modeling of acoustic noise.

are kept consistent across all motors. An exploded view of the SRM, as an example of assembly, is depicted in Fig. 7. The motors are assumed to be face-mounted, with the six inner holes in the first endcap designated for bolt mounting, and a fixed condition is defined for them in the simulation. In addition, for higher accuracy, the contacts between the parts should be defined and the mesh of the different parts should be consistent. Considering the winding in the modal and vibroacoustic analyses is more challenging than the other parts of the structure. In an SRM, each slot is shared by two different coils. Without considering a connection between these coils, each coil would vibrate independently, resulting in numerous additional and unrealistic vibration modes. To mitigate this, it is assumed that all coils are connected, as coils of the same phase are interconnected, causing the windings to vibrate as a single unit. In the case of IPMSM and IM, distributed winding is employed and the end windings on each side are treated as end rings. Table 3 provides the mechanical properties of the materials used in the vibroacoustic analyses [29].

Table 4 provides the results of the modal analysis of the proposed motors, showcasing mode shapes with circumferential orders 0, 2, 3, and 4. The rear endcap is considered for the modal analyses, but it is hidden in the plots to give a view of the inside of the motor. For the analyzed SRM and IM, the natural frequencies of each different mode are rather close. Both motors share the same stack length, and the slight disparity in their natural frequencies can be attributed to differences in stator and winding topologies. However, the IPMSM diverges from this pattern, with a larger difference in natural frequencies, particularly noticeable in higher frequencies (modes 0 and 4). These differences can be attributed to the shorter stack length of the motor.

B. VIBROACOUSTIC ANALYSIS

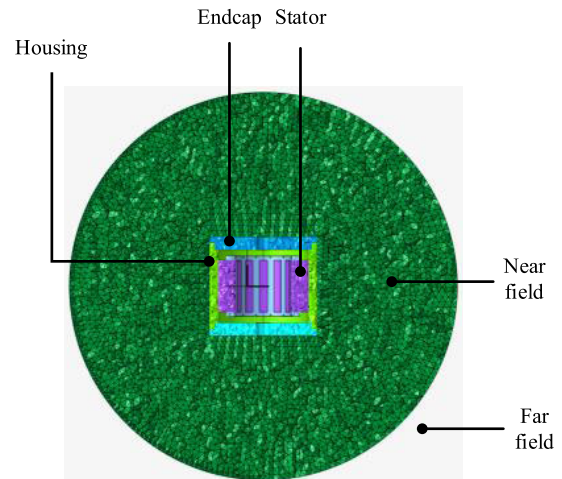When employing numerical techniques to model acoustic noise and vibration, selecting the appropriate element type and element size becomes crucial in balancing accuracy and computational efficiency. For instance, compared to hexahedral elements, tetrahedral elements offer greater adaptability for fitting and meshing complex geometries, resulting in improved mesh quality. Additionally, the use of hexahedral elements can present challenges when transitioning from smaller elements in intricate areas to larger ones elsewhere in the geometry [7]. Hence, tetrahedron elements are used for structural meshing in this study.

The vibroacoustic simulation and analysis in an electric motor comprise three distinct stages: initiating vibrations in the motor structure using electromagnetic forces, transmitting structure-borne noise, and emitting acoustic noise [30]. The accurate acoustic noise simulation at each of these stages hinges on appropriately meshing the structural, near-field, and far-field regions. These regions are illustrated in Fig. 8, which shows the structural and acoustic meshing of the SRM as an example. The near field pertains to the area where sound wave characteristics are influenced by structural vibrations, while the far field is where sound wave properties are influenced by the surrounding medium, such as air. Typically, the near field is represented as the interior of a sphere. To guarantee the precision of the simulation without excessive computational cost, the thickness of this sphere within the near field must be a minimum of one wavelength, as measured from the surface of the housing. The acoustic meshing's element size can be determined by:

$$\varepsilon = \frac{c}{n \times f} \tag{8}$$

where c represents the speed of sound (343 m/s), f is the highest frequency of the acoustic noise, and n is the number of elements per wavelength, which is considered as four, here [26]. In this study, the minimum and maximum frequencies used for acoustic simulations are 1000 Hz and 10 kHz, respectively.

In vibroacoustic analysis, a constant damping ratio is used for each motor, and it can be calculated by:

$$\varsigma_{circ} = \frac{1}{2\pi}(2.76 \times 10^{-5} f_{circ} + 0.062) \quad (9)$$

where ς_{circ} is the modal damping ratio, circ is the circumferential order of the vibration mode, and f_{circ} is the natural frequency of the corresponding mode [29]. In this study, an averaged damping ratio is utilized by averaging the damping ratios of the modes that can be excited for each motor (modes 0 and 4 for SRM, mode 0 for IPM, and modes 0 and 4 for IM).

Notably, the averaged damping ratio values do not incorporate the damping ratio of mode 8. This is due to the natural frequency of mode 8 surpassing 20 kHz, potentially leading to an overestimation of the damping ratio. Table 5 shows the calculated damping ratio values for each motor.

Fig. 9 presents the acoustic noise simulation results for the analyzed motors. In this depiction, the sound pressure level (SPL) waveforms are specifically computed for the rated operating point since shifting to different operating points does not change the pattern of radial force harmonics or the relationship between acoustic noise and radial force harmonics. The validation of peak points within these waveforms is conducted using the previously identified dominant radial force harmonics and natural frequencies, with a separate discussion provided for each motor.

1) SRM

The dominant radial force harmonics exhibit a temporal order of multipliers of 8 for a 12/8 SRM, as illustrated in Fig. 5(a). Lower-order harmonics, with higher amplitudes, result in sharp peaks in the SPL waveform, as depicted in Fig. 9(a). Additionally, harmonics (240,0) and (320,4) excite mode 0 and mode 4, respectively, contributing to a higher noise level near these frequencies. To simulate this motor, a dynamic model is used in MATLAB/SIMULINK which benefits from a hysteresis current controller with a variable frequency. Compared to the other two motors, the noise level difference between dominant and nondominant acoustic noise harmonics is lower in this case. This can be attributed to the current shape of this motor and variable switching frequency, which increases the amplitude of nondominant radial force harmonics.

2) IPMSM

The dominant radial force harmonics in a 48/8 IPMSM exhibit a temporal order of multipliers of 8, as shown in Fig. 5(b). Lower-order harmonics, characterized by higher amplitudes, lead to sharp peaks in the SPL waveform, as depicted in Fig. 9(b). Additionally, harmonic (216,0) excites mode shape 0, contributing to a higher noise level near the related frequency. For the temporal order 48, the noise level of the motor is approximately 70 dB, the highest among the analyzed motors. This can be attributed to the higher amplitude of the radial force harmonic at this frequency.
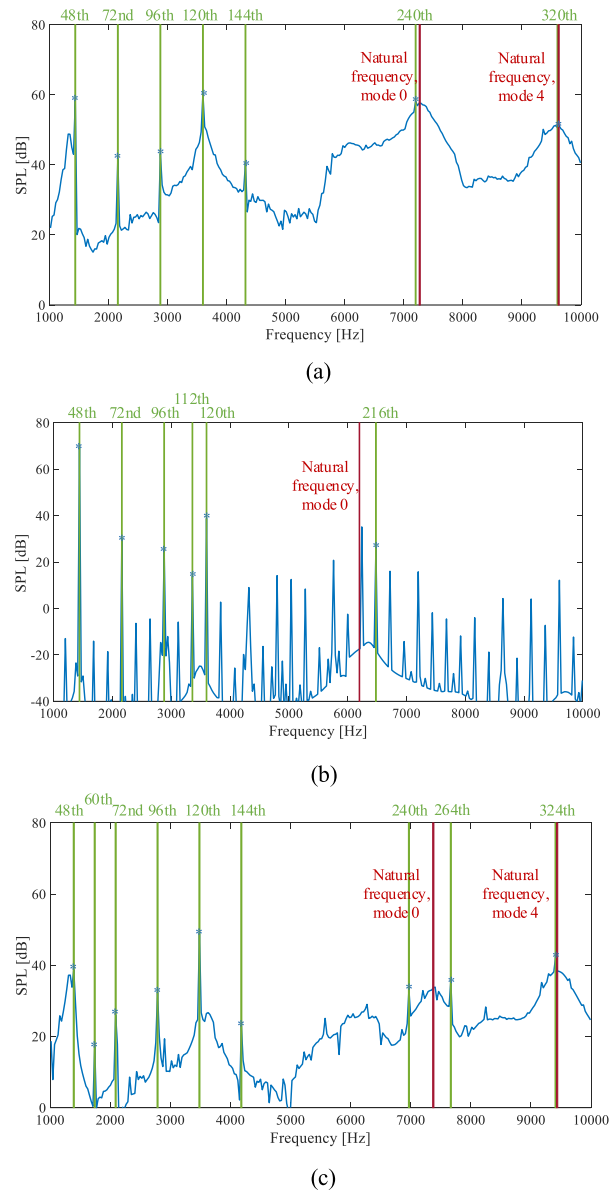

FIGURE 9. Sound pressure level (SPL) of the analyzed motors (a) SRM (b) IPMSM (c) IM.

Another contributing factor can be the different stack lengths of the IPMSM compared to the other two motors. Despite this sharp peak, the overall noise level of this motor is the lowest among the studied cases. It should be noted that a pure sinusoidal excitation is used in analyzing this motor which does not include the PWM harmonics. This is why the amplitudes of nondominant radial force harmonics are low. When the PWM effect is considered, it is anticipated that the difference between the noise level of dominant and nondominant acoustic noise harmonics would be lower.

3) IM

As illustrated in Fig. 5(c), the dominant radial force harmonics exhibit a temporal order of multipliers of 4 for

the analyzed IM. Lower-order harmonics, which have higher amplitudes, result in sharp peaks in the SPL waveform, as shown in Fig. 9(c). Additionally, harmonics (240,0) and (246,0) excite mode shape 0, while harmonic (324,4) excites mode shape 4, contributing to a higher noise level near the related frequency. The difference in amplitude of the dominant and nondominant acoustic noise harmonics is higher than in the IPMSM and lower than in the SRM. Similar to IPMSM, a pure sinusoidal excitation is used in FEA to simulate the IM. However, the number of factors contributing to the harmonic orders is higher for the IM, and the temporal order is a multiplier of 4, unlike the other two motors. Hence, the density of the dominant harmonics is higher for this motor in the same frequency range.

V. CONCLUSION

This paper provides a comparison of the radial force and acoustic noise harmonics of a switched reluctance, an interior permanent magnet, and an induction motor. The electromagnetic performance of these motors is assessed using 2D FEA simulation results. Subsequently, the radial force waveforms and radial force harmonic spectra of the analyzed motors are presented, and a distinct pattern is defined to describe the dominant radial force harmonics of each motor. For the SRM and IM, three factors influence the harmonic orders, whereas two factors influence the harmonic orders in the IPMSM. These factors include the number of stator and rotor poles, as well as the number of phases for the SRM; the number of poles, stator slots, and rotor bars for the IM; and the number of poles and stator slots for the IPMSM. For the IM, the temporal order of the harmonics is a multiple of four, while it is a multiple of eight for the SRM and IPMSM. In addition, the spatial order of the harmonics is a multiple of four for the SRM and IM, and it is a multiple of eight for the IPMSM. Introducing the 3D assembly of the motors, modal analysis is conducted to determine mode shapes and natural frequencies. Finally, the vibroacoustic analysis is performed after discussing its requirements, and the SPL of the analyzed motors is calculated. It is demonstrated that there is a good correlation between the dominant radial force harmonics and peak points in the SPL waveforms of the motors. The vibration mode four is not excited in the IPMSM, unlike the other two motors since the radial force of this motor lacks harmonics with a spatial order of four. Furthermore, the acoustic noise of the IM includes harmonic orders that are multiples of four, whereas, for the other two motors, only harmonic orders that are multiples of eight are perceptible, aligning with the temporal orders of the radial force harmonics.

ACKNOWLEDGMENT

REFERENCES

[1] B. Bilgin and A. Emadi, "Electric motor industry and switched reluctance machines," in *Switched Reluctance Motor Drives*. Boca Raton, FL, USA: CRC Press, Nov. 2018, pp. 1–33.

[2] M. Masoumi, K. Rajasekhara, D. Parati, and B. Bilgin, "Manufacturing techniques for electric motor coils with round copper wires," *IEEE Access*, vol. 10, pp. 130212–130223, 2022.

[3] A. Naina, S. Paryani, and Shri. S. N. Jani, "Comparison between surface-mounted and interior PM motor for EV application," in *Proc. Int. Conf. Intell. Technol. (CONIT)*, Hubli, India, Jun. 2021, pp. 1–6.

[4] J. Wang, W. Geng, J. Guo, L. Li, and Z. Zhang, "Design and performance comparison of novel flux-concentrating IPM machines for power generation system application of extended-range electric vehicle," *IEEE Trans. Ind. Electron.*, vol. 70, no. 5, pp. 4450–4460, May 2023.

[5] Z. Yang, F. Shang, I. P. Brown, and M. Krishnamurthy, "Comparative study of interior permanent magnet, induction, and switched reluctance motor drives for EV and HEV applications," *IEEE Trans. Transport. Electrific.*, vol. 1, no. 3, pp. 245–254, Oct. 2015.

[6] M. E. Abdollahi, A. Zahid, N. Vaks, and B. Bilgin, "Switched reluctance motor design for a light sport aircraft application," *Machines*, vol. 11, no. 3, p. 362, Mar. 2023.

[7] M. E. Abdollahi, N. Vaks, and B. Bilgin, "A multi-objective optimization framework for the design of a high power-density switched reluctance motor," in *Proc. IEEE Transp. Electrific. Conf. Expo. (ITEC)*, Anaheim, CA, USA, Jun. 2022, pp. 67–73.

[8] Z. Q. Zhu, W. Q. Chu, and Y. Guan, "Quantitative comparison of electromagnetic performance of electrical machines for HEVs/EVs," *CES Trans. Electr. Mach. Syst.*, vol. 1, no. 1, pp. 37–47, Mar. 2017.

[9] D. G. Dorrell, A. M. Knight, L. Evans, and M. Popescu, "Analysis and design techniques applied to hybrid vehicle drive machines—Assessment of alternative IPM and induction motor topologies," *IEEE Trans. Ind. Electron.*, vol. 59, no. 10, pp. 3690–3699, Oct. 2012.

[10] L. Vadamodala, S. Das, O. Gundogmus, Y. Sozer, A. Chowdhury, A. W. Bandarkar, S. Harasis, S. M. Chowdhury, E. Haque, T. Husain, F. Venegas, D. Colavincenzo, and J. Geither, "Comparison of electric machine types for electrically driven engine accessories using multiphysics simulation tools," *IEEE Trans. Ind. Appl.*, vol. 57, no. 2, pp. 1399–1410, Mar. 2021.

[11] G. Pellegrino, A. Vagati, B. Boazzo, and P. Guglielmi, "Comparison of induction and PM synchronous motor drives for EV application including design examples," *IEEE Trans. Ind. Appl.*, vol. 48, no. 6, pp. 2322–2332, Nov. 2012.

[12] D. S. Yadav and M. Manisha, "Electric propulsion motors: A comparative review for electric and hybrid electric vehicles," in *Proc. IEEE Int. Conf. Distrib. Comput. Electr. Circuits Electron. (ICDCECE)*, Ballari, India, Apr. 2022, pp. 1–6.

[13] I. Ibrahim, T. Rahman, and D. A. Lowther, "A study of vibroacoustic performance of synchronous motor drives under different operating conditions," in *Proc. IEEE Int. Electric Mach. Drives Conf. (IEMDC)*, Hartford, CT, USA, May 2021, pp. 1–9.

[14] Z. Wu, S. Zuo, Z. Huang, X. Hu, S. Chen, C. Liu, and H. Zhuang, "Effect of Hall errors on electromagnetic vibration and noise of integer-slot inset permanent magnet synchronous motors," *IEEE Trans. Transport. Electrific.*, vol. 9, no. 1, pp. 522–533, Mar. 2023.

[15] A. K. Sahu, A. Emadi, and B. Bilgin, "Noise and vibration in switched reluctance motors: A review on structural materials, vibration dampers, acoustic impedance, and noise masking methods," *IEEE Access*, vol. 11, pp. 27702–27718, 2023.

[16] O. Gundogmus, S. Das, Y. Yasa, M. Elamin, Y. Sozer, J. Kutz, J. Tylenda, and R. L. Wright, "Acoustic noise mitigation in high pole count switched reluctance machines utilizing skewing method on stator and rotor poles," *IEEE Trans. Ind. Electron.*, vol. 69, no. 6, pp. 5581–5593, Jun. 2022.

[17] S.-W. Lee, I.-J. Yang, and W.-H. Kim, "A study on reducing cogging torque of IPMSM applying rotating tapering," *IEEE Trans. Magn.*, vol. 58, no. 8, pp. 1–5, Aug. 2022.

[18] Y. Xiao, Z. Q. Zhu, G. W. Jewell, J. T. Chen, D. Wu, and L. M. Gong, "A novel asymmetric interior permanent magnet synchronous machine," *IEEE Trans. Ind. Appl.*, vol. 58, no. 3, pp. 3370–3382, May 2022.

[19] M. Masoumi, A. Tsao, C. Abeyrathne, A. Sahu, and B. Bilgin, "Investigation of the impact of rotor shaping on the torque and radial force harmonics of a V-shape interior permanent magnet synchronous machine," *IET Electr. Power Appl.*, vol. 18, no. 2, pp. 185–194, Feb. 2024.

[20] A. D. Callegaro, B. Bilgin, and A. Emadi, "Radial force shaping for acoustic noise reduction in switched reluctance machines," *IEEE Trans. Power Electron.*, vol. 34, no. 10, pp. 9866–9878, Oct. 2019.

[21] R. Pupadubsin, B. C. Mecrow, J. D. Widmer, and A. Steven, "Smooth voltage PWM for vibration and acoustic noise reduction in switched reluctance machines," *IEEE Trans. Energy Convers.*, vol. 36, no. 3, pp. 1578–1588, Sep. 2021.

[22] M. L. M. Kimpara, R. R. C. Reis, L. E. B. Da Silva, J. O. P. Pinto, and B. Fahimi, "A two-step control approach for torque ripple and vibration reduction in switched reluctance motor drives," *IEEE Access*, vol. 10, pp. 82106–82118, 2022.

[23] J. Xu and H. Zhang, "Random asymmetric carrier PWM method for PMSM vibration reduction," *IEEE Access*, vol. 8, pp. 109411–109420, 2020.

[24] M. Abdalmagid, M. H. Bakr, and A. Emadi, "A new technique for radial and tangential force calculation time reduction for the optimization process of SRMs," *IEEE Access*, vol. 11, pp. 66076–66093, 2023.

[25] Y. Cai, H. Sobue, C. A. Wiguna, A. Chiba, S. Yoshizaki, and K. Senda, "Radial electromagnetic force estimation using strain gauges in switched reluctance motors," *IEEE Trans. Ind. Appl.*, vol. 59, no. 2, pp. 1242–1252, Mar. 2023.

[26] J. Liang, "Acoustic noise and vibrations in switched reluctance motors: Enhanced modeling," Ph.D. dissertation, Mech. Eng. Dept., McMaster. Univ., Hamilton, ON, USA, 2019.

[27] E. Devillers, M. Hecquet, X. Cimetiere, J.-P. Lecointe, J. L. Besnerais, and T. Lubin, "Experimental benchmark for magnetic noise and vibrations analysis in electrical machines," in *Proc. 13th Int. Conf. Electr. Mach. (ICEM)*, Alexandroupoli, Greece, Sep. 2018, pp. 745–751.

[28] J. Liang, A. D. Callegaro, B. Bilgin, and A. Emadi, "A novel three-dimensional analytical approach for acoustic noise modeling in switched reluctance machines," *IEEE Trans. Energy Convers.*, vol. 36, no. 3, pp. 2099–2109, Sep. 2021.

[29] J. Liang, Y. Li, C. Mak, B. Bilgin, D. Al-Ani, and A. Emadi, "A comprehensive analysis of the acoustic noise in an interior permanent magnet traction motor," in *Proc. IEEE Energy Convers. Congr. Expo. (ECCE)*, Baltimore, MD, USA, Sep. 2019, pp. 3845–3851.

[30] J. O. Fiedler, K. A. Kasper, and R. W. De Doncker, "Calculation of the acoustic noise spectrum of SRM using modal superposition," *IEEE Trans. Ind. Electron.*, vol. 57, no. 9, pp. 2939–2945, Sep. 2010.

MOIEN MASOUMI (Graduate Student Member, IEEE) received the B.Sc. degree in electrical engineering from Tabriz University, Tabriz, Iran, in 2014, and the M.Sc. degree in electrical engineering from the Amirkabir University of Technology, Tehran, Iran, in 2017. He is currently pursuing the Ph.D. degree in electrical engineering with the McMaster Automotive Resource Center (MARC), McMaster University, Hamilton, ON, Canada.

His research interests include design, electromagnetic analysis, and vibroacoustic characterization of electric machines.
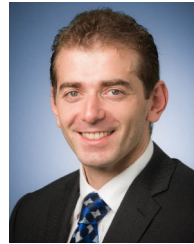
BERKER BILGIN (Senior Member, IEEE) received the Ph.D. degree in electrical engineering from Illinois Institute of Technology, Chicago, IL, USA, in 2011, and the M.B.A. degree from the DeGroote School of Business, McMaster University, Hamilton, ON, Canada, in 2018.

He is currently an Assistant Professor with the Department of Electrical and Computer Engineering (ECE), McMaster University. He is also the Co-Founder and the Vice President of Engineering with Enedym Inc., Hamilton, which is a spin-off company of McMaster University. He specializes in electric machines, electric motor drives (EMDs), advanced controls and software, and virtual engineering. He has authored and coauthored 127 journals and conference papers and three book chapters. He is the Lead Editor and the author of the textbook titled *SRM Drives: Fundamentals to Applications*. He is the Principal Inventor/the Co-Inventor of ten patents and pending patent applications. His current research interests include electric machines, switched reluctance motor (SRM) drives, acoustic noise and vibration analysis and reduction, and power electronics and EMDs. He was the Elected General Chair of the 2016 IEEE Transportation Electrification Conference and Expo (ITEC). He serves as an Associate Editor for IEEE Transactions on Transportation Electrification.

• • •